Cell Reports
Physical Science

CellPress
OPEN ACCESS

Article

Kinetic control over co-self-assembly using an *in situ* dynamic covalent reaction resulting in a synergistic chemo-photodynamic therapy

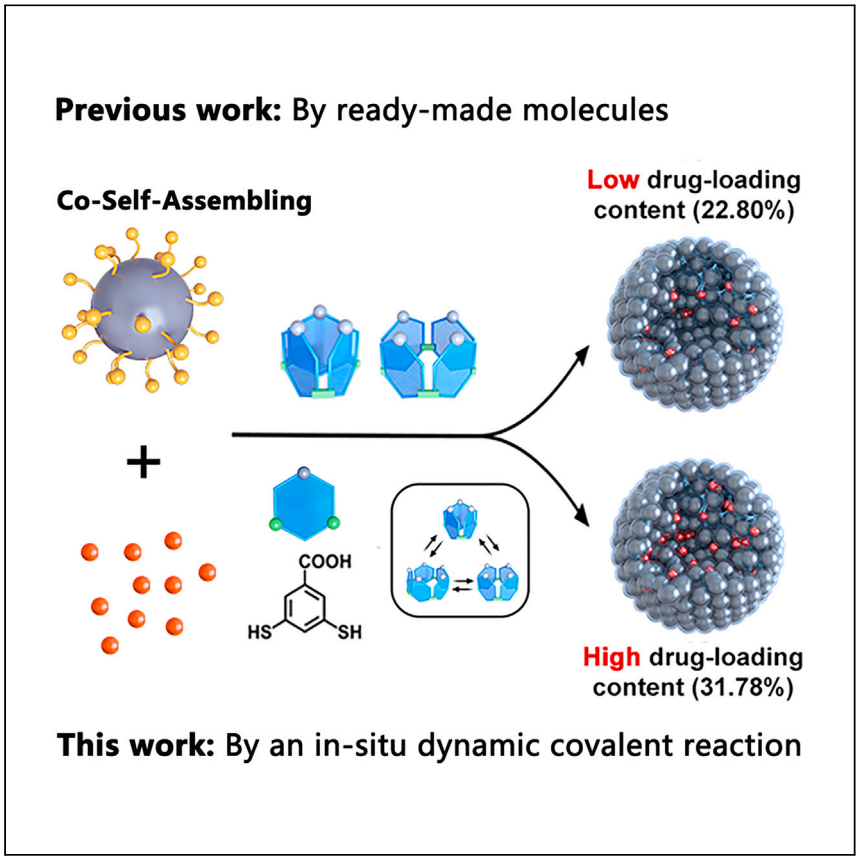

Multicomponent self-assembly holds promise in drug delivery but can be difficult to control. Instead of using ready-made molecules, Wu et al. employ an *in situ* dynamic covalent reaction to kinetically control the co-self-assembly of an inorganic photosensitizer and anticancer drug, yielding stable nanostructures with high drug-loading efficiency and clinical potential for chemo-photodynamic cancer therapy.

Xiaoxia Wu, Jie Xing, Yonglei Lyu, ..., Guoliang Shao, Aiguo Wu, Jianwei Li

aiguo@nimte.ac.cn (A.W.)
jianwei.li@utu.fi (J.L.)

Highlights

Use *in situ* disulfide exchange to kinetically control co-self-assembly

Co-self-assembly produces a co-delivery system of anticancer drugs and photosensitizers

A stable co-delivery system with a high drug-loading content of 31.78%

Smart co-delivery systems for chemo-photodynamic therapy triggered by glutathione

Wu et al., Cell Reports Physical Science 4, 101598
October 18, 2023 © 2023 The Author(s).
https://doi.org/10.1016/j.xcrp.2023.101598

Cell Reports
Physical Science

CellPress
OPEN ACCESS

Article

Kinetic control over co-self-assembly using an *in situ* dynamic covalent reaction resulting in a synergistic chemo-photodynamic therapy

Xiaoxia Wu,[1,4] Jie Xing,[3] Yonglei Lyu,[1,2] Jingjing Yu,[1] Jinghui Yang,[1,2] Dawei Qi,[1] Xin Wang,[1,2] Jie Lin,[3] Guoliang Shao,[4] Aiguo Wu,[3,*] and Jianwei Li[1,5,6,*]

SUMMARY

Multicomponent self-assembly offers a strategy to explore ordered, complex, and dynamic nanosystems and to harness the property of the whole system beyond that of each subcomponent. However, the spontaneous nature of co-self-assembly makes control of the process difficult. Here, we use a thiol-disulfide exchange reaction as an *in situ* dynamic covalent reaction to slowly produce disulfide macrocycles that subsequently trigger the co-self-assembly with an anticancer drug and a photosensitizer. The gradual concentration growth of products shows kinetic control over the concentration of self-assembling disulfides, resulting in a stable co-delivery nanosystem with high drug-loading efficiency (31.78%) and encapsulation efficiency (95.91%). The nanosystem possesses biocompatibility, tumor-accumulating ability, and biosafety and shows a synergistic chemotherapeutic and photodynamic anticancer effect *in vitro* and *in vivo*. Our findings suggest that *in situ* dynamic covalent chemistry advances control over co-self-assembly, paving the way to more functional nanosystems with potential applications in biomedicine, electronics, and renewable energy.

INTRODUCTION

Molecular self-assembly has been playing significant roles in exploring functional nanosystems for a wide range of applications in catalysis, sensing, and biomedicine.[1,2] A typical example is to fabricate drug delivery systems in which carrier molecules and drug molecules self-assemble into nanocarriers through noncovalent interactions.[3] In order to efficiently and effectively deliver anticancer drug molecules to tumor sites, an ideal nanosystem should be stable during the transportation to cancer cells while also being responsive to releasing the encapsulated drug in the tumor microenvironment.[4] Moreover, the nanosystem should also be in an optimal dimension range of 100–200 nm to achieve the enhanced permeability and retention (EPR) effect in target solid tumors.[5,6] Last but not the least, the drug-loading content and encapsulation efficiency of the nanosystem should be high, which can reduce the side effects brought by the carrier molecule and enhance the efficacy of the drug molecule.[7] To equip a single drug delivery nanosystem with all the above-mentioned advantages at the same time, many efforts have been made to develop a large number of carrier molecules by interplaying their affinity between the two components.[8] Unfortunately, the development remains unsatisfactory due to the difficulty in controlling the spontaneous process in molecular self-assembly.[9]

[1]MediCity Research Laboratory, University of Turku, Tykistökatu 6, 20520 Turku, Finland

[2]Department of Chemistry, University of Turku, Vatselankatu 2, 20014 Turku, Finland

[3]Cixi Institute of Biomedical Engineering, International Cooperation Base of Biomedical Materials Technology and Application, Chinese Academy of Science (CAS) Key Laboratory of Magnetic Materials and Devices & Zhejiang Engineering Research Center for Biomedical Materials, Ningbo Institute of Materials Technology and Engineering, CAS, 1219 ZhongGuan West Road, Ningbo 315201, China

[4]Department of Interventional Radiology, The Cancer Hospital of the University of Chinese Academy of Sciences (Zhejiang Cancer Hospital), Institute of Basic Medicine and Cancer (IBMC), Chinese Academy of Sciences (CAS), Hangzhou 310022, China

[5]Hainan Provincial Key Lab of Fine Chem, Key Laboratory of Advanced Materials of Tropical Island Resources of Ministry of Education, Hainan University, Haikou 570228, China

[6]Lead contact

*Correspondence: aiguo@nimte.ac.cn (A.W.), jianwei.li@utu.fi (J.L.)

https://doi.org/10.1016/j.xcrp.2023.101598

This is an open access article under the CC BY-NC-ND license (http://creativecommons.org/licenses/by-nc-nd/4.0/).

This becomes even more challenging when developing a co-delivery system for combination therapy, arising from the increased complexity resulting from more components participating in the self-assembling process.[10,11] Chemo-photodynamic therapy is a typical example of combination therapy, and it has been proven to be a promising co-delivery nanosystem-based approach to cancer treatment.[12] Together with anticancer drugs for a chemotherapy, quantum dots (QDs) are a type of representative photosensitizer used for a photodynamic therapy (PDT). They can damage cancer cells by oxidizing crucial biomacromolecules that absorb near-infrared (NIR) light and effectively generate reactive oxygen species (ROS).[13] For the preparation of the co-delivery nanosystem, carrier molecules are designed and synthesized to mediate the self-assembly.[14] Through noncovalent binding with the ligands attached on the surface of QDs, carrier molecules trigger the aggregation of well-dispersed QDs into nanostructures.[15,16] As the aggregation is performed in aqueous solutions, drug molecules are encapsulated due to hydrophobic effects during the process.[17] However, it is tricky to design the carrier molecule. Thermodynamically, the affinity between the carrier molecule and the ligands on the QDs should be strong enough to support the formation of a stable nanocarrier.[8] Yet, if the binding is too strong, the size of the resulting nanocarrier would be over the optimized dimension for the EPR effect. From a kinetic perspective, the strong binding enables the self-assembly to occur very quickly, resulting in limited loading amounts of drug molecules.[18] Moreover, in most previously reported examples, the carrier molecules are ready made and are mixed with drug molecules and QDs at the same time, leaving very narrow windows to show control over the spontaneous co-self-assembling process.[19–21] Consequently, the development of co-delivery nanosystems has been struggling with two main issues: low drug-loading efficiency and poor stability in the extracellular matrix or tumor microenvironment, which leads to nanocarriers aggregation or disassembly, uncontrollable drug release in the extracellular matrix of tumor tissue, and drug leakage during the delivery process.[4]

Here, rather than using a ready-made carrier molecule, we used an *in situ* dynamic covalent chemical reaction to slowly produce carrier molecules that could bind with the ligands on the surface of QDs and thereby trigger the onset of co-self-assembly to make a co-delivery nanosystem (shown in Figure 1). Using this strategy, the monomer of building block **1** participated the dynamic covalent reaction *in situ* and gradually produced the disulfide macrocycles that triggered the self-assembly of the QDs. However, the addition of ready-made disulfide macrocycles instantly induced the self-assembly. Thus, the gradual increase in the concentration of the carrier molecule represented a strategy for kinetic control over the concentration of the self-assembling molecules, which could give sufficient time to allow self-correction to occur during the reversible process of the chemical reaction and co-self-assembly. This ensured that the system reached an equilibrium and produced a stable self-assembled nanostructure with maximum drug-loading content at the end of the reaction. Specifically, the thiol-disulfide exchange reaction was utilized as the dynamic covalent chemistry to generate the carrier molecules. Doxorubicin (DOX) and Ag_2S QDs were chosen as the anticancer drug and the photosensitizer to create the co-delivery nanosystem for the chemo-photodynamic therapy, respectively. The drug-loading content (31.78%) and the encapsulation efficiency (95.91%) of the co-delivery system were both much higher than previously reported values.[19–22] The resulting co-delivery system exhibited strong cellular uptake and pH and glutathione (GSH)-controlled drug release in human breast cancer cells (MCF-7 cells) and a synergistic chemo-photodynamic therapeutic effect under irradiation with an NIR laser at 808 nm. This treatment effect was confirmed *in vivo*; the co-delivery system was found to have antitumor activity in an MCF-7 cell-derived

CellPress
OPEN ACCESS

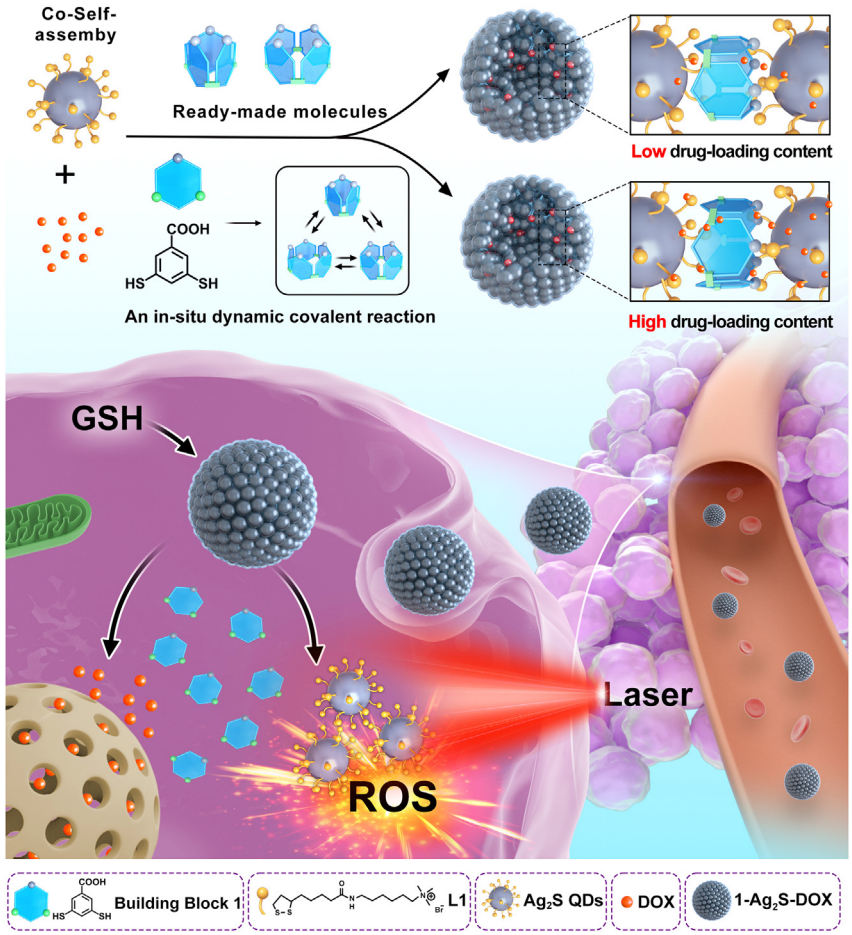

Figure 1. Illustration of co-delivery system for chemo-photodynamic therapy

The multicomponent self-assembly triggered by an *in situ* dynamic covalent reaction into a co-delivery system (**1-Ag_2S-DOX**) that had chemo-photodynamic cancer therapy *in vitro* and *in vivo*.

breast cancer in a xenograft mouse model. Moreover, the co-delivery system showed good biocompatibility, and the side effects of DOX during the treatment were significantly reduced. These findings suggest that *in situ* dynamic covalent chemical reactions could be new tools to give control over co-self-assembly in multicomponent systems, providing new approaches to exploring powerful co-delivery nanosystems for a chemo-photodynamic therapy in this article and more functional nanosystems for a broad range of applications spanning from catalysis and electronics to renewable energy in the future.

RESULTS AND DISCUSSION

Design and verification of the DCS strategy

Ag_2S QDs are semiconductor nanomaterials with the ability to generate ROS; hence, they can potentially be combined with drugs to form co-delivery systems for chemotherapy and PDT in cancer treatment.[23] Thus, Ag_2S QDs were chosen to make the combinatorial therapeutic agent for the target cancer. First, we attached the positively charged ligand **L1**, a quaternary ammonium salt, to the surface of Ag_2S QDs (for synthesis and characterization details, see the supplemental information and Figures S1–S3). The disulfide bonds of **L1** could offer the sulfur source to form

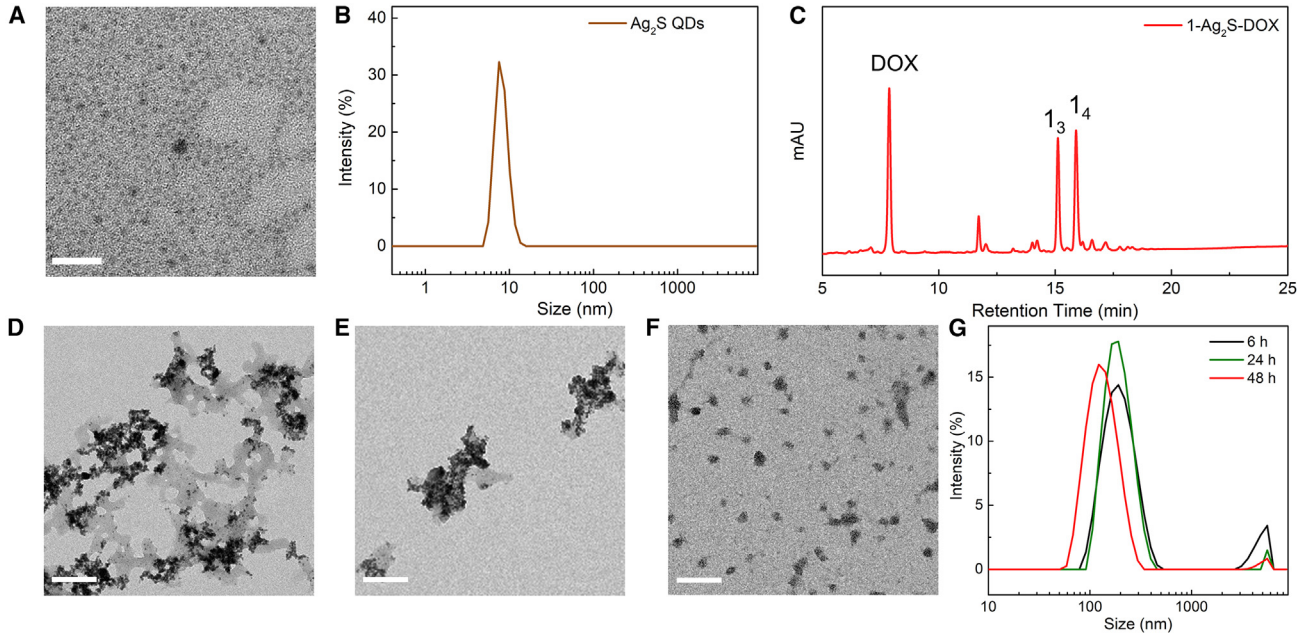

Figure 2. The self-assembly of co-delivery system

(A) Transmission electron microscopy (TEM) images of Ag_2S QDs. Scale bar: 25 nm.

(B) Size distributions of Ag_2S QDs measured by dynamic light scattering (DLS).

(C) High-performance liquid chromatography (HPLC) analysis of the reactive delivery system **1-Ag_2S-DOX** after building block **1** was fully oxidized.

(D–F) TEM images of the co-delivery system during the loading process at different times: 6 (D), 24 (E), and 48 h (F). Scale bar: 200 nm.

(G) Size distribution of the **1-Ag_2S-DOX** nanoparticles with different drug-loading times measured by DLS at room temperature.

Ag_2S QDs. Its ammonium groups with positive charges could provide the potential electrostatic interaction with the deprotonated carboxylic acids of building block **1**, which may promote the formation of self-assembled nanostructures. Additionally, the hydrophobicity of the alkyl chain in **L1** could benefit the loading of hydrophobic anticancer drugs in the co-delivery system.[9] Due to the charge repulsion between the QDs, the obtained Ag_2S QDs were adequately dispersed in an aqueous solution, and transmission electron microscopy (TEM) analysis showed that they had an average diameter of around 4 nm (see Figure 2A). This size was confirmed by the dynamic light scattering (DLS) results that the hydrodynamic diameter was around 6 nm (Figure 2B).

Our strategy involved loading the drug DOX into nanoparticles as they were being formed by the QDs noncovalently associating with the carrier molecules generated by the building block through a dynamic covalent reaction. The most striking difference between our approach and previous approaches is that the concentration of the carrier molecules should gradually increase as the dynamic covalent chemical reaction progresses.[24] Thus, the reaction rate should be slow, but the reaction yield should be high. In the context of biomedical applications, the reaction should also be biocompatible. We reason that the thiol-disulfide exchange reaction is an ideal candidate that can meet all these requirements.[25] Disulfide bonds are ubiquitous in protein structures and can slowly form via the oxidation of thiols by oxygen in the air under physiological conditions. In addition, when a sufficient amount of oxygen is present, the formation of disulfide bonds from thiols can be quantified.[26] Therefore, we equipped dithiol building block **1** with a carboxylic acid group with the aim of producing dynamic ring-like carrier molecules with negative charges

that could noncovalently associate with positively charged **L1** on the surface of Ag_2S QDs via host-guest interactions.

To verify whether our strategy could result in a high drug-loading content, we prepared a series of the target reactive delivery systems of **1-Ag_2S-DOX** using various concentrations of the dithiol building block **1**, Ag_2S QDs, and DOX in phosphate-buffered saline (PBS; pH 7.4) to calculate drug-loading efficiency according to the standard curve of DOX (Figure S4). The maximum drug-loading efficiency (31.78%) and the corresponding encapsulation efficiency (95.91%) were obtained after slow oxidation over 2 days using the following combination of reagents: 0.75 mM building block **1**, 0.1 mM Ag_2S QDs (the concentration of **L1** on Ag_2S QDs), and 0.2 mM DOX. This combination showed a significantly higher loading capacity than previously reported co-delivery systems that used ready-made templates.[27] The components of **1-Ag_2S-DOX** have been analyzed and calculated using nuclear magnetic resonance (NMR), inductively coupled plasma optical emission spectrometry (ICP-OES), and high-performance liquid chromatography (HPLC) in Figure 2C. The concentrations of Ag^+, **L1**, **1**, and DOX were 2, 0.4, 0.38, and 0.78 mM, respectively. Four systems of Ag_2S-DOX (prepared from Ag_2S QDs and DOX), **1-Ag_2S** (prepared from Ag_2S QDs and building block **1**), building block **1**, and 1-DOX (prepared from building block **1** and DOX) were used as controls in the multicomponent system (shown in Figure S5).

We also prepared a pre-oxidized co-delivery system as another control by mixing Ag_2S QDs (0.1 mM **L1**) and DOX (0.2 mM) in a solution containing disulfide macrocycles that were identical to those found in the reactive system **1-Ag_2S-DOX**: 1_3 (0.096 mM) and 1_4 (0.095 mM). However, the drug-loading efficiency and corresponding encapsulation efficiency for this system were 22.80% and 89.32%, respectively, which were lower than those of **1-Ag_2S-DOX**. Meanwhile, we also prepared a titrated pre-oxidized co-delivery system using a flow pump as another control by continuously and slowly adding pre-formed macrocycles into the Ag_2S QDs and DOX mixtures. The resulting drug-loading content and corresponding encapsulation efficiency of this titrated pre-oxidized system were 19.16% and 85.06%, respectively, which were similar to those obtained by the previous control experiments where disulfide macrocycles were added in one portion, suggesting that the direct addition of ready-made disulfide macrocycles resulted in lower loading efficiencies of the co-delivery systems. These results demonstrate that using *in situ* dynamic covalent chemistry is a powerful strategy to enhance the drug-loading capacity, which resulted from the kinetic control over the concentration growth of the carrier molecules that triggered the co-self-assembly process in the multicomponent system.

Unraveling the mechanism behind the strong loading capacity

To better understand the drug loading directed by the *in situ* dynamic covalent reaction, we first monitored the morphological changes in the **1-Ag_2S-DOX** system using TEM and DLS. For this, samples were taken 6, 24, and 48 h after the reaction was initiated, and TEM images of the samples were recorded. The initial sample was cloudy, as the Ag_2S QDs started to aggregate immediately (Figure 2D). As the oxidative reaction proceeded, the solution turned clear again, and the TEM analysis showed that the size of the aggregates became smaller (Figure 2E) and that the aggregates changed to monodispersed nanoparticles with a diameter of approximately 60 nm at the end of the reaction (Figure 2F). This size was confirmed by DLS analysis, which showed that the hydrodynamic diameter was about 70 nm (Figure 2G). We also studied the morphological changes in a pre-oxidized co-delivery

system by TEM and DLS at different reaction times of 6, 24, and 48 h in Figure S6. The TEM analysis showed that the size of the aggregates increased with the increase of reaction time (Figures S6A–S6C), which was opposite to that in **1-Ag_2S-DOX** system. These sizes were also confirmed by DLS analysis, which showed that the hydrodynamic diameters increased in the range of 300–800 nm (Figure S6D). In addition, HPLC analysis indicated that the concentration of the disulfide macrocycles ($\mathbf{1}_3$ and $\mathbf{1}_4$) in the **1-Ag_2S-DOX** system rose with time (Figure S7). The compositional change in the reactive co-delivery system with time was investigated by HPLC, as shown in Figure S8. It could be found that the content of $\mathbf{1}_3$ and $\mathbf{1}_4$ macrocycles in the **1-Ag_2S-DOX** system increased with the increase of oxidation time in the first 24 h and reached a balance within 48 h, suggesting that the dynamic covalent chemical reaction reached up to an equilibrium in self-assembly shown in Figure S8A. In addition, we also analyzed the content of $\mathbf{1}_3$ and $\mathbf{1}_4$ macrocycles in the **1** system shown in Figure S8B. It seemed that building block **1** had slower oxidation than that in the **1-Ag_2S-DOX** system, which was attributed to the oxidation effect from DOX and the template effect of DOX and the Ag_2S QDs. These results suggested a clear morphological transformation of the nanostructures during the dynamic covalent self-assembly (DCS) process, showing that the self-assembling process was kinetically controlled by the gradual concentration increase of the disulfide macrocycles ($\mathbf{1}_3$ and $\mathbf{1}_4$).

Because the TEM analysis showed that the resulting individual **1-Ag_2S-DOX** nanocarriers were formed by the aggregation of several Ag_2S QDs, we reasoned that the noncovalent interaction between the macrocycle and **L1** on the surface of Ag_2S QDs was the main driving force for the formation of a nanocarrier. We then elucidated the noncovalent interaction responsible for the formation of **1-Ag_2S-DOX** using NMR. As the NMR signal of **L1** on the QDs was poor, we used a model compound, cetyltrimethylammonium bromide (CTAB), to analyze the noncovalent interaction between the macrocycle and Ag_2S QDs (Figure S9A). When $\mathbf{1}_3$ and $\mathbf{1}_4$ were mixed with CTAB in deuterium water (D_2O; PBS, pH 7.4), the signals of the methylene protons H_3, H_4, and H_5 of CTAB that were next to the N^+ head group had remarkable upfield shifts due to the shielding effect arising from the negative charge of the deprotonated carboxylic acid group and the electron-rich cavity of the macrocycle. These results revealed that the disulfide macrocycle was threaded by the ligand with the inclusion of the part close to the quaternary ammonium salt.[24] In addition, two-dimensional nuclear Overhauser spectroscopy (2D-NOESY) was also tested to understand the spatial conformation of the resulting inclusion complex (Figure S9B). The nuclear Overhauser effect (NOE) correlation signals were observed between protons H_a and H_b on the disulfide macrocycles and the methylene protons H_2 and H_3 (or H_4 and H_5) that were next to the N^+ head group, confirming the abovementioned threading binding mode.[24] In order to verify the threading binding mode, a control experiment was designed by using benzoic acid (BA) to replace the macrocycles in the same PBS buffer (pH 7.4). We analyzed its 1D-^{1}H NMR and 2D-NOESY spectra in Figure S10. It could be found that the signal of the protons H_3, H_4, and H_5 of CTAB next to the N^+ head group moved upfield because of the electrostatic interaction between the CTAB and BA (Figure S10A). However, no NOE correlation signal was observed between protons H_a, H_b, and H_c of BA and protons H_3, H_4, and H_5 of CTAB (Figure S10B). These results suggest that the CTAB was unlikely contacted with the aromatic ring of BA, further proving the threading binding mode in CTAB and disulfide macrocycle system. Given that DOX is usually buried in the hydrophobic pocket of liposomes, we concluded that it was encapsulated by the alkyl chain of the ligands during the noncovalent interaction between the macrocycles and the Ag_2S QDs.

In Figure S11, it was also found that the hydrodynamic diameter of the **1-Ag_2S** nanoparticles was about 110 nm, which was larger than the 80 nm of the **1-Ag_2S-DOX** nanoparticles (Figure S11E). Hence, the encapsulation of DOX reduced the size of the assembled structures—a feature that likely contributed to the formation of the well-dispersed delivery system (in Figures S11C and S11D). Together, these findings suggest that using an *in situ* dynamic covalent reaction provided kinetic control over the complex co-self-assembling process, representing a powerful approach to preparing nanocarriers that contain both QDs and drugs for cancer treatment.

Anticancer properties of the nanocarriers prepared by DCS

The hydrodynamic diameter of the nanoparticles was determined to be approximately 80 nm (Figure S11E). Meanwhile, the stability of the co-delivery system in a physiological environment was tested by DLS (Figure S12). The size of **1-Ag_2S-DOX** in fetal bovine serum (FBS) was larger than that in PBS and DMEM, which was attributed to the formation of protein corona on the surface of nanostructures.[28,29] In addition, the hydrodynamic diameter of **1-Ag_2S-DOX** was in the range of 200–250 nm, which was an ideal size for delivery to tumor tissue via the EPR effect.[5] Furthermore, TEM imaging of **1-Ag_2S-DOX** in FBS for 2 days also indicated that there was no obvious size increase of **1-Ag_2S-DOX**, which could confirm the formation of protein corona on the surface of nanostructures in Figure S13. Then, the zeta potentials of the Ag_2S QDs, the **1-Ag_2S** nanoparticles, and the **1-Ag_2S-DOX** nanoparticles were measured as +19.30, −17.43, and −33.83 mV, respectively (Figure S11F). The zeta potential of the Ag_2S QDs was positive due to the positively charged quaternary ammonium group of the attached ligand. After interacting with the deprotonated carboxylic acid groups of the disulfide macrocycles, the zeta potential decreased and became more negative after drug loading. It is expected that the negative charge of the drug-loaded nanocarriers would decrease the occurrence of nonspecific interactions between the nanoparticles and cells.[30]

To further investigate the application of the co-delivery system in chemo-photodynamic therapy, we characterized their physicochemical properties. The UV-visible (UV-vis) spectrum of **1-Ag_2S-DOX** showed a strong absorption peak of DOX at 480 nm. Compared with the absorption intensity of the sample that only contained Ag_2S QDs at the same concentration, the absorption intensity of the typical peak at 808 nm was enhanced (Figure S11G), showing that **1-Ag_2S-DOX** has potential in PDT under irradiation by an NIR light. In Figure S14, the compositional change in the reactive co-delivery system under the treatment of GSH was investigated by HPLC. HPLC analysis of the **1-Ag_2S-DOX** with GSH (5 mM) sample revealed that the content of $\mathbf{1}_3$ and $\mathbf{1}_4$ macrocycles decreased and dissociated into monomers of building block **1** at 8.31 min, which slightly overlap with the peak of DOX (8.12 min), further confirming the stimuli-responsive disassembly and intelligent drug release.

In addition, the controllable drug-release performance of the **1-Ag_2S-DOX** nanosystem was evaluated by investigating the release of DOX in PBS (pH 7.4 or 5.5) with and without GSH (2 mM). As shown in Figure 3A, at pH 5.5 and in the presence of GSH (2.0 mM), the percentages of DOX that were cumulatively released reached 60.5% and 77.0% after 24 and 48 h of incubation, respectively. The percentages were lower (42.1% and 55.0%) at pH 7.4 with GSH. However, in the absence of GSH, the cumulative amounts of DOX released at the same time points were significantly lower: 12.6% and 23.7% at pH 7.4 and 16.0% and 25.5% at pH 5.5. These results indicated that the addition of GSH notably facilitated the drug release and that

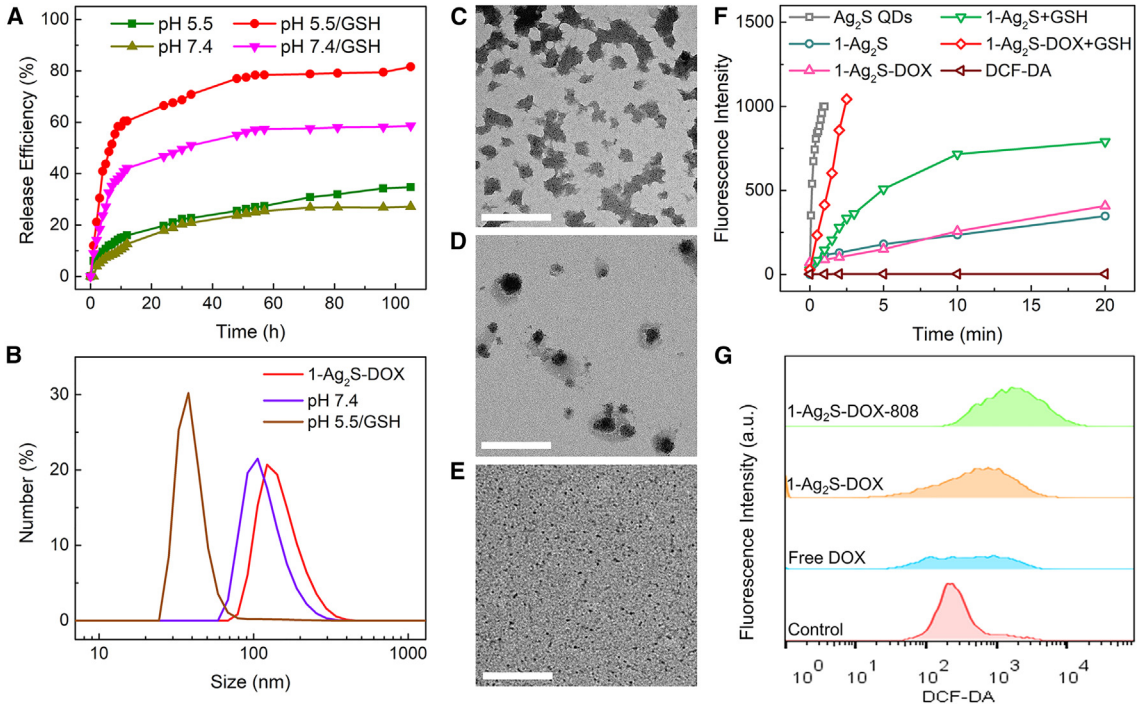

Figure 3. The stimulus-responsive drug-release performance of co-delivery system

(A) DOX release curves of **1-Ag_2S-DOX** in PBS (pH 7.4 or 5.5) with and without GSH (2 mM).

(B) Size distribution of the **1-Ag_2S-DOX** nanoparticles and samples after drug release, as measured by DLS.

(C–E) TEM images of **1-Ag_2S-DOX** samples after drug release in PBS at pH 7.4 (C), 5.5 (D), and 5.5 (E) with GSH. Scale bar: 200 nm.

(F) ROS detection using DCFH-DA under irradiation (808 nm, 1 W/cm^2) for different Ag_2S samples with and without GSH (2 mM).

(G) Intracellular ROS detection in MCF-7 cells incubated with free DOX and **1-Ag_2S-DOX** (DOX concentration of 5 μg/mL) with and without irradiation (808 nm, 1 W/cm^2, 1 min).

the value of pH only affected the drug-release performance in the presence of GSH.[31]

The size distribution of the **1-Ag_2S-DOX** nanocarrier after drug release was also investigated using DLS and TEM (Figures 3B–3E). Nanoparticle size decreased significantly after drug release triggered by GSH, suggesting that the co-delivery system was disassembled, resulting in smaller-sized nanoparticles. This change was attributed to the breakage of disulfide macrocycles, as the HPLC analysis of the **1-Ag_2S-DOX** with GSH sample revealed that the macrocycles were reduced to building block **1**.[32] Therefore, considering the microenvironment of tumor cells, this nanocarrier with GSH- and pH-triggered drug-release functionality holds promise as a cancer therapy agent. Moreover, this co-delivery system may persist for a long period in the blood and may achieve rapid renal clearance after drug release and break down into smaller particles, which may also solve the degradation problems associated with metal nanomaterials.[14]

To estimate the PDT potential of **1-Ag_2S-DOX**, the generation of ROS during irradiation with an NIR laser at 808 nm was studied. 2,7-Dichlorodi-hydrofluorescein diacetate (DCFH-DA) is a fluorescent probe that is oxidized to the intensively fluorescent 2,7-dichlorodi-fluorescein (DCF) by ROS. During irradiation, the generated amount of ROS increased in all samples that contained Ag_2S QDs, suggesting that photocatalytic activity was triggered by the excitation at 808 nm (Figures 3F and S15).[33]

When the ability of generating ROS was compared among the samples, the Ag_2S QD sample was more active than the **1-Ag_2S** and **1-Ag_2S-DOX** samples. This revealed a decreased ROS production, attributable to the neutralization of the positive charges on the nanocarriers by the deprotonated carboxylic groups of the disulfide macrocycles, thereby reducing their ability to seize unpaired electrons.[34] Under the treatment of GSH, the ROS generation ability of **1-Ag_2S-DOX** enhanced significantly because of the disassembly of self-assembled nanoparticles. The released Ag_2S QDs had positive charges that could more easily capture unpaired electrons and consequently achieve higher ROS generation.[24] Thus, it could achieve smart PDT in tumor cells with a high level of GSH concentration.[24] This was demonstrated by the generation of intracellular ROS in MCF-7 cells incubated with **1-Ag_2S-DOX** (DOX concentration of 5 μg/mL) using flow cytometry and confocal laser scanning microscopy (CLSM). The fluorescence of DCF was considerably more intense in irradiated MCF-7 cells than in nonirradiated cells (Figure 3G). Yet, there was no obvious fluorescence in MCF-7 cells alone (control group) or in MCF-7 cells incubated with free DOX (free DOX group). CLSM images of generated ROS in cells further confirmed the results in the flow cytometry test (in Figure S16). These results indicate that **1-Ag_2S-DOX** could be used as a photosensitizer in PDT with NIR irradiation at 808 nm.

In vitro biocompatibility and cellular uptake of the co-delivery system

Biocompatibility is a critical factor for all nanomedicine delivery systems.[35] Hence, the cytotoxicity of each component (excluding DOX) of **1-Ag_2S-DOX** was first evaluated *in vitro* via the thiazolyl blue tetrazolium bromide (MTT) assay (Figure 4A).[31] The viability of MCF-7 cells was above 84% when they were incubated for 24 h with the **1-Ag_2S** nanoparticles at concentrations ranging from 0.4 to 80 μg/mL. However, the Ag_2S QDs were deemed cytotoxic, and this was due to their positive surface charge. These results suggest that the negatively charged disulfide macrocycles effectively interacted with and neutralized the surface charge of the Ag_2S QDs, resulting in a nanocarrier with low cytotoxicity and excellent biocompatibility. Therefore, **1-Ag_2S-DOX** has potential as a drug delivery system.

DOX inhibits nucleic acid synthesis and exhibits antitumor activity when delivered to the nucleus of tumor cells.[36,37] Thus, it was essential to evaluate the cellular uptake and localization of **1-Ag_2S-DOX**. First, the cellular uptake was investigated using flow cytometry. The fluorescence emission images were recorded between 550 and 660 nm for DOX with excitation at 480 nm. The DOX fluorescence in MCF-7 cells incubated with **1-Ag_2S-DOX** (**1-Ag_2S-DOX** group) was more intense than that in MCF-7 cells incubated without (control group) and with free DOX (free DOX group) (Figure 4B), indicating that **1-Ag_2S-DOX** could enter the cancer cells more easily than the free drug. This result was confirmed when CLSM images of MCF-7 cells incubated with free DOX and **1-Ag_2S-DOX** for 1 h were analyzed. Furthermore, significantly more DOX was present in the nucleus of MCF-7 cells in the **1-Ag_2S-DOX** group compared with in the free DOX group (Figure 4C). To have a better understanding of the excellent drug delivery capacity of **1-Ag_2S-DOX**, we also monitored the cellular uptake and delivery over a range of periods using CLSM. Both the cellular uptake and the accumulation of DOX in the nucleus increased with incubation time, up to the 60 min time point (Figures S17 and S18). These results further demonstrated the applicability of **1-Ag_2S-DOX** as an anticancer drug delivery system.

In vitro chemo-photodynamic therapy

The performance of **1-Ag_2S-DOX** as a chemo-photodynamic therapeutic agent was evaluated by MTT assay. First, its activity as a chemotherapeutic agent (without

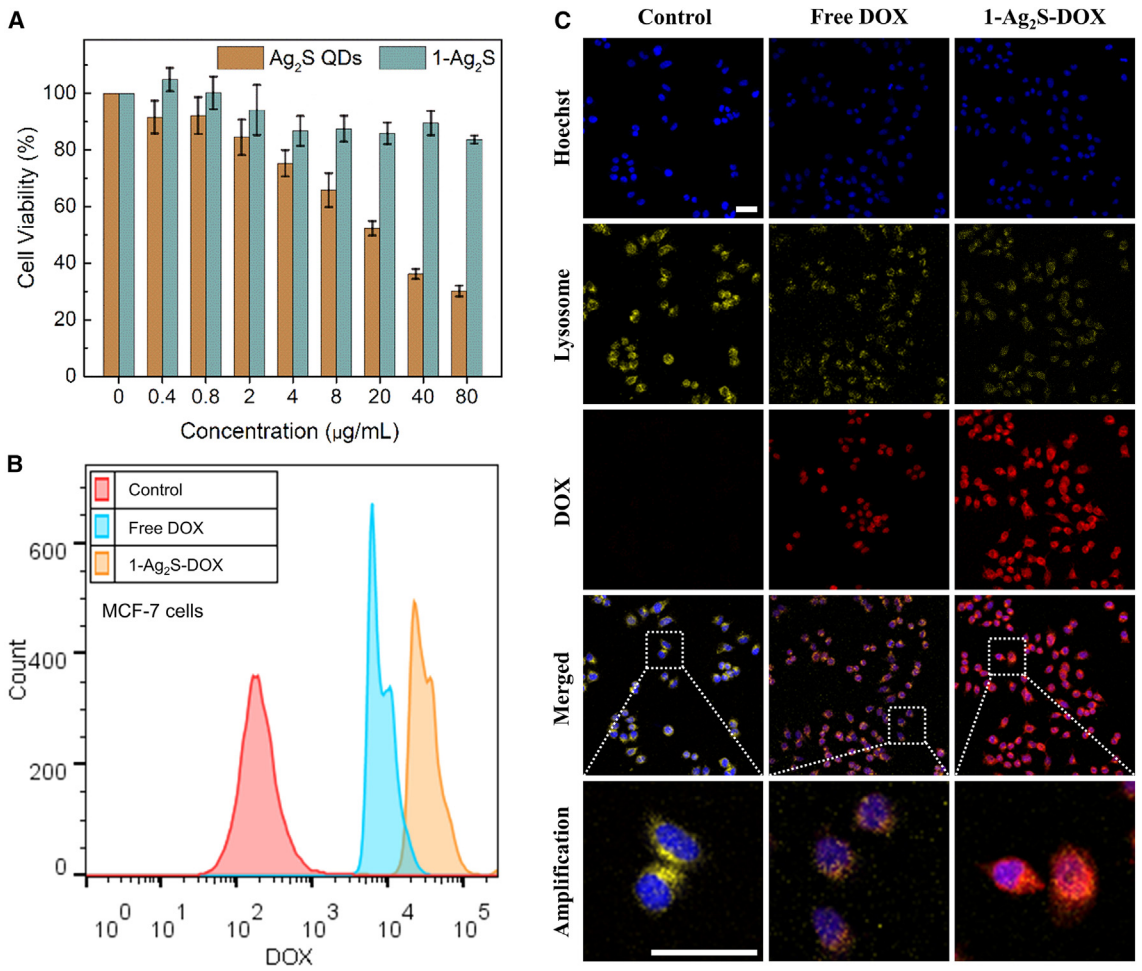

Figure 4. *In vitro* biocompatibility and uptake of co-delivery system in MCF-7 cells

(A) Cell viabilities of Ag_2S QDs and **1-Ag_2S** incubated with MCF-7 cells at different concentrations. Error bars shown represent the SD (mean ± SD, n = 6).

(B) Flow cytometry curves of DOX fluorescence in MCF-7 cells incubated with free DOX and **1-Ag_2S-DOX**.

(C) CLSM images of MCF-7 cells incubated with free DOX and **1-Ag_2S-DOX** (DOX concentration of 5 μg/mL) for 60 min. MCF-7 cells incubated without DOX were used as a control. The cells were treated with Hoechst 33342 and LysoTracker Deep Red to stain the nucleus and lysosome, respectively. Scale bars: 50 μm.

irradiation) against MCF-7 cells was investigated (Figures 5A and 5B). MCF-7 cells were incubated with free DOX or **1-Ag_2S-DOX** for 24, 48, or 72 h. The viability of cells exposed to **1-Ag_2S-DOX** was lower than that of cells exposed to the free DOX group with the same DOX concentration and incubation time. Furthermore, the half maximal inhibitory concentration (IC_{50}) of free DOX was 10.83 μg/mL and of **1-Ag_2S-DOX** was 2.97 μg/mL (see the table in Figure 5D), indicating that **1-Ag_2S-DOX** has a better chemotherapeutic effect than free DOX.

We also evaluated the combined chemo-photodynamic therapeutic performance of **1-Ag_2S-DOX** in MCF-7 cells (Figure 5C). Under laser irradiation at 808 nm (1 W/cm^2, 20 s), the MCF-7 cells incubated with **1-Ag_2S** (**1-Ag_2S** group) for 24 h showed a reasonably high viability of 52.7%. However, under the same irradiation conditions, the viability of cells exposed to **1-Ag_2S-DOX** was 17.1%, which was lower than that of cells exposed to **1-Ag_2S-DOX** without irradiation (23.2%). In addition, the IC_{50} of **1-Ag_2S-DOX** with irradiation was 1.83 μg/mL, which was about 5.9 times lower than

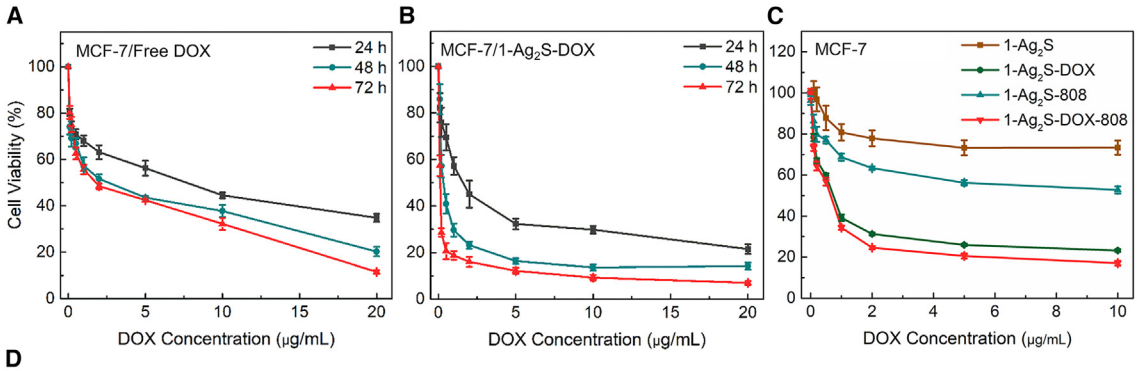

D

Samples	Free DOX	1-Ag_2S-DOX	1-Ag_2S-DOX-808
IC_{50} (μg/mL)	10.829	2.973	1.83

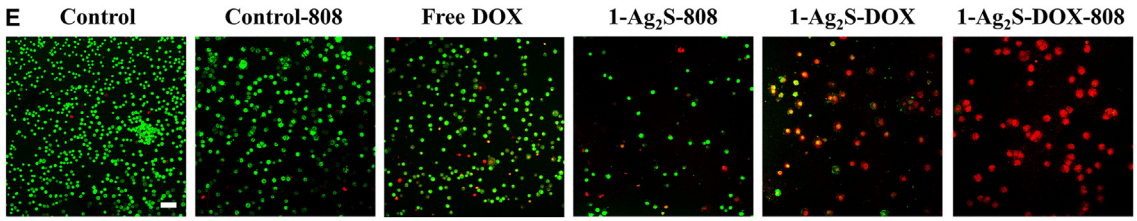

Figure 5. ***In vitro*** **chemo-photodynamic therapy of co-delivery system**

(A–C) Cell viabilities of MCF-7 cells incubated with (A) free DOX, (B) **1-Ag_2S-DOX**, and (C) **1-Ag_2S-DOX** without and with irradiation (808 nm, 1 W/cm^2, 20 s). Error bars shown represent the SD (mean ± SD, n = 6).

(D) Table of calculated half maximal inhibitory concentration (IC_{50}) of free DOX, **1-Ag_2S-DOX**, and **1-Ag_2S-DOX-808** groups incubated with MCF-7 cells for 24 h.

(E) Fluorescence images of MCF-7 cells incubated with different samples (DOX concentration: 5 μg/mL) with or without 808 nm irradiation (1 W/cm^2, 1 min). The MCF-7 cells were treated by calcein-AM and propidium iodide (PI) dyes to stain live and dead cells. Scale bar: 100 μm.

that of free DOX (Figure 5D). At low concentrations of **1-Ag_2S-DOX**, chemotherapy accounted for the majority of synergistic therapy, but the effect of dual therapy can also be far greater than that of chemotherapy alone. Moreover, dead/live cell images treated with **1-Ag_2S-DOX** under 808 nm irradiation were also studied to evaluate antitumor ability in Figure 5E. From the imaging of dead/live cells, it could be found that the number of living cells in the group of **1-Ag_2S-DOX-808** was far less than that of other groups, which is consistent with results in the MTT assay, further proving the excellent chemo-photodynamic therapeutic ability of **1-Ag_2S-DOX** in MCF-7 cells. The above findings indicate that **1-Ag_2S-DOX** may have a significant chemo-photodynamic therapeutic effect against tumor cells.

Apoptosis induced by **1-Ag_2S-DOX** was also investigated using flow cytometry (Figure S19). The early and late apoptotic cells constituted 3.81 ± 0.16% of the population when MCF-7 cells were treated with DOX alone, while the percentage increased to 5.33 ± 0.59% when cells were treated with **1-Ag_2S-DOX** without irradiation and to 11.97 ± 0.60% when cells were treated with **1-Ag_2S-DOX** under irradiation. Cell viability was higher in the apoptosis test compared with that in the MTT assay, which resulted from different experimental conditions of shorter incubation times and lower DOX concentrations to minimize the interference of DOX fluorescence on the propidium iodide (PI) probe. Therefore, under the light of 808 nm, **1-Ag_2S-DOX** showed both enhanced apoptotic and antiproliferation activities

compared with DOX alone, indicating a good chemo-photodynamic effect to inhibit tumor proliferation.

In vivo biocompatibility and chemo-photodynamic therapeutic effect

Next, we examined the chemo-photodynamic therapeutic effect of **1-Ag_2S-DOX** against tumors *in vivo* and its clinical potential. For this, we studied the antitumor effect of **1-Ag_2S-DOX** in a mouse model. First, the *in vivo* biocompatibility was evaluated in Institute of Cancer Research (ICR) mice. After tail vein injection of free DOX, **1-Ag_2S**, or **1-Ag_2S-DOX**, the major organs of the mice were removed and stained with hematoxylin and eosin (H&E) to check the pathological outcomes of the delivery of the molecules (Figure S20). In mice that received free DOX, minor elevations in leukocyte infiltration were observed in the alveolar areas of the lungs, and there were pathological lesions in the heart and liver. By comparison, there were no obvious lesions in the heart, spleen, lungs, or kidneys of mice that received **1-Ag_2S-DOX**, indicating that encapsulating DOX in **1-Ag_2S-DOX** could reduce its toxicity. Hematology analysis was also assessed using blood samples from ICR mice as shown in Figure S21. It could be found that there was no obvious influence on the major markers in hematology analysis under the injection of the co-delivery system, indicating that **1-Ag_2S-DOX** has superior biocompatibility and potential as a drug delivery system.

Secondly, to monitor the accumulation of the co-delivery system, an NIR fluorescent dye of IR-783 was loaded into co-delivery system. *In vivo* fluorescence distributions and *in vitro* fluorescence images of tumors and major organs after injection of free IR-783 and **1-Ag_2S-DOX** marked with IR-783 (**1-Ag_2S-DOX-783**) are shown in Figure S22. It could be found that the fluorescence signal in the tumor site of the **1-Ag_2S-DOX-783** group increased with the time and reached the maximum at 24 h and maintained at a high level, as shown in Figures S22A and S22B, indicating the superior tumor-accumulating ability of **1-Ag_2S-DOX**. As displayed in Figures S22C and S22D, the fluorescence image and the average fluorescence intensity of tumors and major organs at 24 h post-injections showed that the tumor accumulation signal of **1-Ag_2S-DOX** was significantly higher than the free IR-783 group, which further confirmed the tumor-accumulating ability. Hence, we conclude that this co-delivery system possesses good biocompatibility and tumor-accumulating ability, which is a criterion for any cancer treatment agent.

Given the excellent *in vitro* antitumor activity of **1-Ag_2S-DOX**, the *in vivo* antitumor activity was assessed using an MCF-7 xenograft model in BALB/c-nu mice (n = 4). Groups of mice were injected via the tail vein three times with either DOX, **1-Ag_2S-DOX**, or PBS on days 0, 4, and 8. Some of the groups were subjected to irradiation (NIR laser, 808 nm, 2 W/cm^2, 5 min) the day after each injection (e.g., the **1-Ag_2S-DOX-808** group). The body weight and tumor volume of each mouse were measured as shown in Figures 6A–6C. Tumor-bearing mice in the **1-Ag_2S-DOX** and **1-Ag_2S-DOX-808** groups had no obvious weight loss or death during the treatment (Figures 6A and 6B), indicating that the nanocarrier did not cause serious side effects during the treatment period.[24] In contrast, the tumors in the mice injected with PBS grew uncontrollably (Figure 6C). The tumors in mice treated with **1-Ag_2S-DOX** grew at a slower rate than those in mice treated with free DOX, indicating that **1-Ag_2S-DOX** had a chemotherapeutic effect.

Irradiation seemed to have enhanced the anticancer effect of **1-Ag_2S-DOX**, as evidenced by the results of the **1-Ag_2S-DOX-808** group compared with the free DOX group and the **1-Ag_2S-DOX** group. This finding was confirmed by the tumor weights and images, as shown in Figures 6D and 6E. From these results, it could be

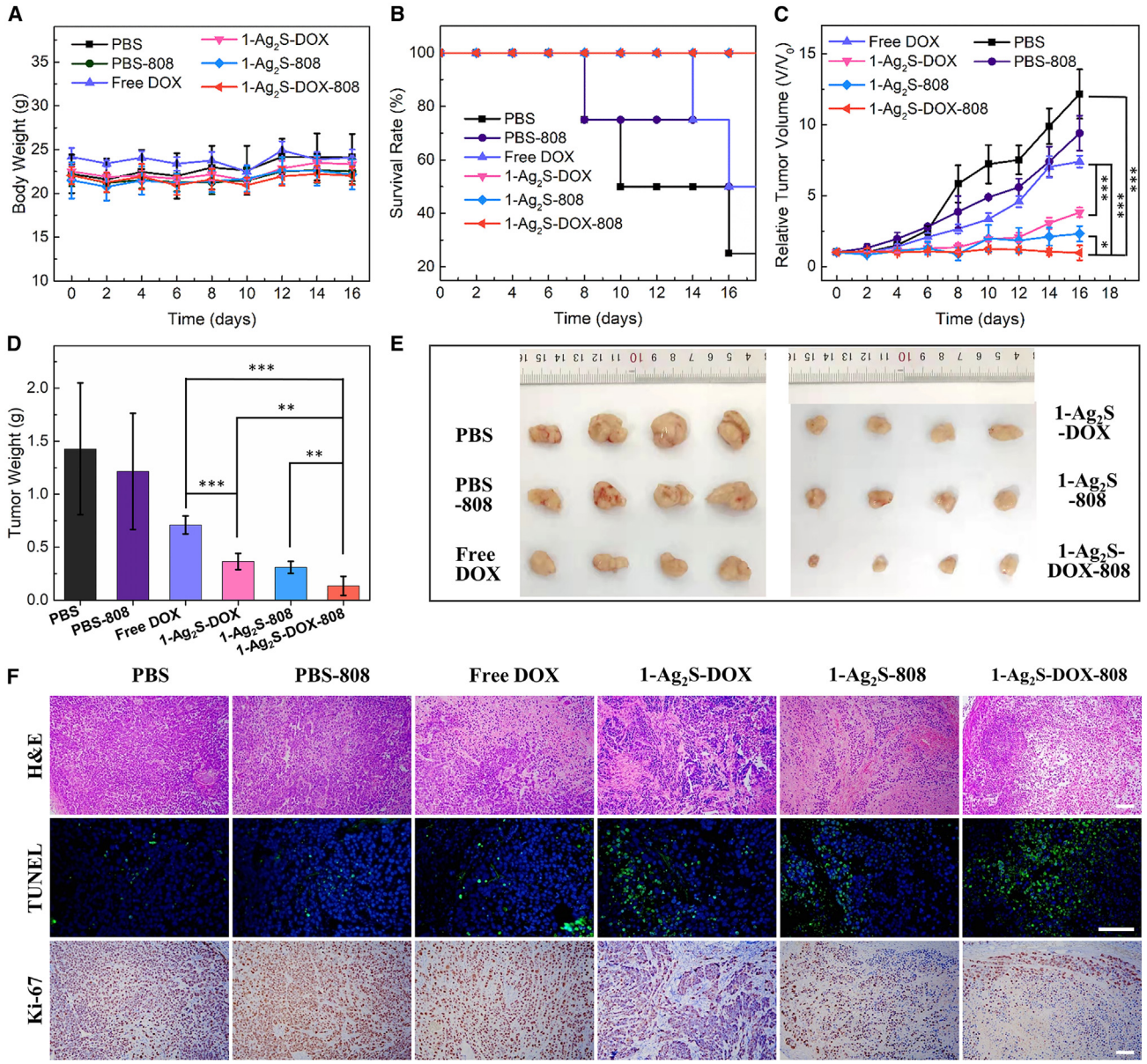

Figure 6. *In vivo* chemo-photodynamic therapy of co-delivery system

(A) Changes in body weight of MCF-7 tumor-bearing mice during the treatments with PBS, PBS-808, free DOX, **1-Ag_2S-DOX**, **1-Ag_2S-808**, or **1-Ag_2S-DOX-808**. PBS with or without irradiation and free DOX were used as controls. The irradiation condition: 808 nm, 2 W/cm^2, 5 min.

(B) Survival curve of tumor-bearing mice after different treatments with various formulations.

(C) Relative tumor-growth curves during treatment with various formulations.

(D and E) Tumor weight and tumor photographs after different treatments with various formulations.

(F) Hematoxylin and eosin (H&E), terminal deoxynucleotidyl transferase dUTP nick end labeling (TUNEL), and Ki-67 staining of tumors from mice that received various formulations after 12 days of treatment. Scale bars: 100 μm. Error bars shown represent the SD (mean ± SD, n = 4, *p < 0.05, **p < 0.01, ***p < 0.001).

concluded that the mice that received **1-Ag_2S-DOX** and underwent irradiation exhibited the most tumor inhibition, confirming the synergistic effects of PDT and chemotherapy. Moreover, H&E, terminal deoxynucleotidyl transferase dUTP nick end labeling (TUNEL), and Ki-67 protein staining of tumor slices were utilized to analyze the antitumor effects of **1-Ag_2S-DOX** (Figure 6F). Clearly, **1-Ag_2S-DOX**

and irradiation caused more extensive apoptosis and necrosis than the other treatments, indicating the tumor inhibition activity of this chemo-photodynamic therapeutic agent.[38] Together, these results demonstrate that **1-Ag_2S-DOX** coupled with irradiation has synergistic chemotherapy and PDT activity against cancer *in vivo*.

To investigate the systemic toxicity of **1-Ag_2S-DOX** toward cancer cells in BALB/c-nu mice, we selected the following standard hematology markers for analysis in Figure S23.[39] From the hematology results, it can be concluded that **1-Ag_2S-DOX** treatment and irradiation did not influence any of the markers (except for platelets [PLTs], which were affected by irradiation, as shown in the PBS-808 and **1-Ag_2S-808** groups' results in Figure S23B). As shown in Figure S24, there was no significant histopathological damage observed in the H&E-stained organs, which further confirmed the biological safety of **1-Ag_2S-DOX** *in vivo*. The above results jointly confirm that **1-Ag_2S-DOX** has superior biocompatibility and potential as a drug delivery system with synergistic chemotherapy and PDT application in cancer treatment. Therefore, the strategy of using an *in situ* dynamic covalent reaction offers an efficient and effective solution for the preparation of co-delivery systems for combination therapy, opening a new door in the development of dynamic nanosystems with a wide range of potential applications in biomedicine, catalysis, electronics, and renewable energy.

In this study, we have used an *in situ* dynamic covalent chemical reaction to trigger the co-self-assembly in a multicomponent system, which resulted in an innovative co-delivery system with improved drug-loading efficiency and stability and controllable drug release for chemo-photodynamic therapy against cancer. We have also demonstrated that the dynamic covalent reaction showed real-time control over the concentration growth of the hub molecule in the co-self-assembly for the co-delivery system. The resulting co-delivery system (**1-Ag_2S-DOX**) had a high DOX loading efficiency (31.78%) and encapsulation efficiency (95.91%). Its intelligent drug-release functionality enabled the release of DOX to be triggered by GSH and the acidic microenvironment within tumor cells. In the presence of GSH, the amount of DOX released could be controlled by adjusting the pH, achieving stimuli-responsive drug release at the target location in tumor tissues. The nanocarrier also facilitated cellular uptake, efficiently delivering DOX to the nucleus of tumor cells, and showed synergistic chemotherapeutic and photodynamic therapeutic effects against cancer cells *in vitro*. Its antitumor effects were also observed *in vivo*. Moreover, the nanosystem also exhibited biocompatibility, tumor-accumulating ability, and reduced side effects. Therefore, the strategy of using an *in situ* dynamic covalent reaction offers an efficient and effective solution for the preparation of co-delivery systems for combination therapy, opening a new door in the development of dynamic nanosystems with a wide range of potential applications in biomedicine, catalysis, electronics, and renewable energy.

EXPERIMENTAL PROCEDURES

Resource availability

Lead contact

Further information and requests for resources and reagents should be directed to and will be fulfilled by the lead contact, Jianwei Li (jianwei.li@utu.fi).

Materials availability

This study did not generate new unique materials.

Data and code availability

All data generated during the study are available from the lead contact upon reasonable request. This study did not generate a code.

Experimental methods

All methods including preparation of co-delivery system, drug release, and ROS detection and details of biocompatibility and chemo-photodynamic therapy *in vitro* and *in vivo* can be found in the supplemental experimental procedures.

SUPPLEMENTAL INFORMATION

Supplemental information can be found online at https://doi.org/10.1016/j.xcrp.2023.101598.

ACKNOWLEDGMENTS

The authors thank Markus Peurla (Laboratory Engineer, Institute of Biomedicine) and the Cell Imaging and Cytometry Core (Turku Bioscience Center, Turku, Finland) for help with TEM characterization and imaging/flow cytometry analysis. This work is financially supported by the National Natural Science Foundation of China (nos. 22161016, 82202274, 82072032, 32025021, 52002380, and 31971292); the Ningbo 3315 Innovative Teams Program (grant no. 2019A-14-C); the Fellowship of China Postdoctoral Science Foundation (2021M692872 and 2022M723206); project funding (no. 318524) from the Academy of Finland; and a fellowship from the Sigrid Jusélius Foundation.

AUTHOR CONTRIBUTIONS

X. Wu designed and performed the main experiments and wrote the manuscript. J.X. performed partial animal corresponding assays and data analysis. Y.L., J. Yu, J. Yang, D.Q., and X. Wang contributed to data analysis of HPLC and NMR. J. Lin and G.S. provided important insights and revised the manuscript. A.G. and J.L. provided foundational guidance on experimental design. J. Li designed the study, performed the analysis, and co-wrote the manuscript.

DECLARATION OF INTERESTS

The authors declare no competing interests.

Received: June 18, 2023
Revised: August 7, 2023
Accepted: September 5, 2023
Published: September 26, 2023

REFERENCES

1. Li, J., Anraku, Y., and Kataoka, K. (2020). Self-boosting catalytic nanoreactors integrated with triggerable crosslinking membrane networks for initiation of immunogenic cell death by pyroptosis. Angew. Chem., Int. Ed. *59*, 13526–13530. https://doi.org/10.1002/anie.202004180.

2. Li, L., Yang, Z., and Chen, X. (2020). Recent advances in stimuli-responsive platforms for cancer immunotherapy. Acc. Chem. Res. *53*, 2044–2054. https://doi.org/10.1021/acs.accounts.0c00334.

3. Min, H.S., Kim, H.J., Naito, M., Ogura, S., Toh, K., Hayashi, K., Kim, B.S., Fukushima, S., Anraku, Y., Miyata, K., and Kataoka, K. (2020). Systemic brain delivery of antisense oligonucleotides across the blood–brain barrier with a glucose-coated polymeric nanocarrier. Angew. Chem., Int. Ed. *59*, 8173–8180. https://doi.org/10.1002/anie.201914751.

4. Wankar, J., Kotla, N.G., Gera, S., Rasala, S., Pandit, A., and Rochev, Y.A. (2020). Recent advances in host–guest self-assembled cyclodextrin carriers: implications for responsive drug delivery and biomedical engineering. Adv. Funct. Mater. *30*, 1909049. https://doi.org/10.1002/adfm.201909049.

5. Aslan, K., Gryczynski, I., Malicka, J., Matveeva, E., Lakowicz, J.R., and Geddes, C.D. (2005). Metal-enhanced fluorescence: an emerging tool in biotechnology. Curr. Opin. Biotechnol. *16*, 55–62. https://doi.org/10.1016/j.copbio.2005.01.001.

6. Longmire, M., Choyke, P.L., and Kobayashi, H. (2008). Clearance properties of nano-sized particles and molecules as imaging agents: considerations and caveats. Nanomedicine *3*, 703–717. https://doi.org/10.2217/17435889.3.5.703.

7. Shi, J., Kantoff, P.W., Wooster, R., and Farokhzad, O.C. (2017). Cancer nanomedicine: progress, challenges and opportunities. Nat. Rev. Cancer *17*, 20–37. https://doi.org/10.1038/nrc.2016.108.

8. Yang, C., Lin, Z.I., Chen, J.A., Xu, Z., Gu, J., Law, W.C., Yang, J.H.C., and Chen, C.K. (2022). Organic/inorganic self-assembled hybrid nano-architectures for cancer therapy applications. Macromol. Biosci. *22*, 2100349. https://doi.org/10.1002/mabi.202100349.

9. Kwon, N., Kim, H., Li, X., and Yoon, J. (2021). Supramolecular agents for combination of photodynamic therapy and other treatments. Chem. Sci. *12*, 7248–7268. https://doi.org/10.1039/D1SC01125A.

10. Wu, D., Li, B.L., Zhao, Q., Liu, Q., Wang, D., He, B., Wei, Z., Leong, D.T., Wang, G., and Qian, H. (2020). Assembling defined DNA nanostructure

with nitrogen-enriched carbon dots for theranostic cancer applications. Small *16*, 1906975. https://doi.org/10.1002/smll.201906975.

11. Rival, J.V., Nonappa, and Shibu, E.S. (2020). Light-triggered reversible supracolloidal self-assembly of precision gold nanoclusters. ACS Appl. Mater. Interfaces *12*, 14569–14577. https://doi.org/10.1021/acsami.0c00328.

12. Pham, T.C., Nguyen, V.-N., Choi, Y., Lee, S., and Yoon, J. (2021). Recent strategies to develop innovative photosensitizers for enhanced photodynamic therapy. Chem. Rev. *121*, 13454–13619. https://doi.org/10.1021/acs.chemrev.1c00381.

13. Zhang, H., Wang, T., Liu, H., Ren, F., Qiu, W., Sun, Q., Yan, F., Zheng, H., Li, Z., and Gao, M. (2019). Second near-infrared photodynamic therapy and chemotherapy of orthotopic malignant glioblastoma with ultra-small $Cu_{2-x}Se$ nanoparticles. Nanoscale *11*, 7600–7608. https://doi.org/10.1039/C9NR01789E.

14. Hu, X., Sun, J., Li, F., Li, R., Wu, J., He, J., Wang, N., Liu, J., Wang, S., Zhou, F., et al. (2018). Renal-clearable hollow bismuth subcarbonate nanotubes for tumor targeted computed tomography imaging and chemoradiotherapy. Nano Lett. *18*, 1196–1204. https://doi.org/10.1021/acs.nanolett.7b04741.

15. Li, M., Luo, Z., and Zhao, Y. (2018). Self-assembled hybrid nanostructures: versatile multifunctional nanoplatforms for cancer diagnosis and therapy. Chem. Mater. *30*, 25–53. https://doi.org/10.1021/acs.chemmater.7b03924.

16. Ozin, G.A., Hou, K., Lotsch, B.V., Cademartiri, L., Puzzo, D.P., Scotognella, F., Ghadimi, A., and Thomson, J. (2009). Nanofabrication by self-assembly. Mater. Today *12*, 12–23. https://doi.org/10.1016/S1369-7021(09)70156-7.

17. Yang, Y., Sun, B., Zuo, S., Li, X., Zhou, S., Li, L., Luo, C., Liu, H., Cheng, M., Wang, Y., et al. (2020). Trisulfide bond–mediated doxorubicin dimeric prodrug nanoassemblies with high drug loading, high self-assembly stability, and high tumor selectivity. Sci. Adv. *6*, eabc1725. https://doi.org/10.1126/sciadv.abc1725.

18. Fang, R., Liu, M., and Jiang, L. (2020). Design of nanoparticle systems by controllable assembly and temporal/spatial regulation. Adv. Funct. Mater. *30*, 1903351. https://doi.org/10.1002/adfm.201903351.

19. Xiao, Z., Zuo, W., Chen, L., Wu, L., Liu, N., Liu, J., Jin, Q., Zhao, Y., and Zhu, X. (2021). H_2O_2 self-supplying and GSH-depleting nanoplatform for chemodynamic therapy synergetic photothermal/chemotherapy. ACS Appl. Mater. Interfaces *13*, 43925–43936. https://doi.org/10.1021/acsami.1c10341.

20. Mei, K.-C., Liao, Y.-P., Jiang, J., Chiang, M., Khazaieli, M., Liu, X., Wang, X., Liu, Q., Chang, C.H., Zhang, X., et al. (2020). Liposomal delivery of mitoxantrone and a cholesteryl indoximod prodrug provides effective chemo-immunotherapy in multiple solid tumors. ACS Nano *14*, 13343–13366. https://doi.org/10.1021/acsnano.0c05194.

21. Cai, Z., Zhang, Y., He, Z., Jiang, L.-P., and Zhu, J.-J. (2020). NIR-triggered chemo-photothermal therapy by thermosensitive gold nanostar@mesoporous silica@liposome-composited drug delivery systems. ACS Appl. Bio Mater. *3*, 5322–5330. https://doi.org/10.1021/acsabm.0c00651.

22. Han, R., Liu, Q., Lu, Y., Peng, J., Pan, M., Wang, G., Chen, W., Xiao, Y., Yang, C., and Qian, Z. (2022). Tumor microenvironment-responsive Ag_2S-PAsp(DOX)-cRGD nanoparticles-mediated photochemotherapy enhances the immune response to tumor therapy. Biomaterials *281*, 121328. https://doi.org/10.1016/j.biomaterials.2021.121328.

23. Jiang, W., Wu, Z., Yue, X., Yuan, S., Lu, H., and Liang, B. (2015). Photocatalytic performance of Ag2S under irradiation with visible and near-infrared light and its mechanism of degradation. RSC Adv. *5*, 24064–24071. https://doi.org/10.1039/C4RA15774E.

24. Cao, Y., Yang, J., Eichin, D., Zhao, F., Qi, D., Kahari, L., Jia, C., Peurla, M., Rosenholm, J.M., Zhao, Z., et al. (2021). Self-synthesizing nanorods from dynamic combinatorial libraries against drug resistant cancer. Angew. Chem., Int. Ed. *60*, 3062–3070. https://doi.org/10.1002/anie.202010937.

25. Li, J., Nowak, P., and Otto, S. (2013). Dynamic combinatorial libraries: from exploring molecular recognition to systems chemistry. J. Am. Chem. Soc. *135*, 9222–9239. https://doi.org/10.1021/ja402586c.

26. Lam, R.T.S., Belenguer, A., Roberts, S.L., Naumann, C., Jarrosson, T., Otto, S., and Sanders, J.K.M. (2005). Amplification of acetylcholine-binding catenanes from dynamic combinatorial libraries. Science *308*, 667–669. https://doi.org/10.1126/science.1109999.

27. Hu, X.-Y., Gao, J., Chen, F.-Y., and Guo, D.-S. (2020). A host-guest drug delivery nanosystem for supramolecular chemotherapy. J. Contr. Release *324*, 124–133. https://doi.org/10.1016/j.jconrel.2020.05.008.

28. Weber, C., Morsbach, S., and Landfester, K. (2019). Possibilities and limitations of different separation techniques for the analysis of the protein corona. Angew. Chem., Int. Ed. *58*, 12787–12794. https://doi.org/10.1002/anie.201902323.

29. Yu, Y., Luan, Y., and Dai, W. (2022). Dynamic process, mechanisms, influencing factors and study methods of protein corona formation. Int. J. Biol. Macromol. *205*, 731–739. https://doi.org/10.1016/j.ijbiomac.2022.03.105.

30. Wu, X., Luo, L., Yang, S., Ma, X., Li, Y., Dong, C., Tian, Y., Zhang, L., Shen, Z., and Wu, A. (2015). Improved SERS nanoparticles for direct detection of circulating tumor cells in the blood. ACS Appl. Mater. Interfaces *7*, 9965–9971. https://doi.org/10.1021/acsami.5b02276.

31. Pan, Y., Zhang, L., Zeng, L., Ren, W., Xiao, X., Zhang, J., Zhang, L., Li, A., Lu, G., and Wu, A. (2016). Gd-based upconversion nanocarriers with yolk-shell structure for dual-modal imaging and enhanced chemotherapy to overcome multidrug resistance in breast cancer. Nanoscale *8*, 878–888. https://doi.org/10.1039/C5NR06522D.

32. Xuan, W., Xia, Y., Li, T., Wang, L., Liu, Y., and Tan, W. (2020). Molecular self-assembly of bioorthogonal aptamer-prodrug conjugate micelles for hydrogen peroxide and pH-independent cancer chemodynamic therapy. J. Am. Chem. Soc. *142*, 937–944. https://doi.org/10.1021/jacs.9b10755.

33. Zheng, D.-W., Li, B., Li, C.-X., Fan, J.-X., Lei, Q., Li, C., Xu, Z., and Zhang, X.-Z. (2016). Carbon-dot-decorated carbon nitride nanoparticles for enhanced photodynamic therapy against hypoxic tumor via water splitting. ACS Nano *10*, 8715–8722. https://doi.org/10.1021/acsnano.6b04156.

34. Wu, X., Yang, L., Luo, L., Shi, G., Wei, X., and Wang, F. (2019). Engineered g-C_3N_4 quantum dots for tunable two-photon imaging and photodynamic therapy. ACS Appl. Bio Mater. *2*, 1998–2005. https://doi.org/10.1021/acsabm.9b00055.

35. Sun, T., Zhang, Y.S., Pang, B., Hyun, D.C., Yang, M., and Xia, Y. (2014). Engineered nanoparticles for drug delivery in cancer therapy. Angew. Chem., Int. Ed. *53*, 12320–12364. https://doi.org/10.1002/anie.201403036.

36. Kankala, R.K., Liu, C.G., Chen, A.Z., Wang, S.B., Xu, P.Y., Mende, L.K., Liu, C.L., Lee, C.H., and Hu, Y.F. (2017). Overcoming multidrug resistance through the synergistic effects of hierarchical pH-sensitive, ROS-generating nanoreactors. ACS Biomater. Sci. Eng. *3*, 2431–2442. https://doi.org/10.1021/acsbiomaterials.7b00569.

37. Lin, G., Mi, P., Chu, C., Zhang, J., and Liu, G. (2016). Inorganic nanocarriers overcoming multidrug resistance for cancer theranostics. Adv. Sci. *3*, 1600134. https://doi.org/10.1002/advs.201600134.

38. Li, H., Qian, K., Zhang, H., Li, L., Yan, L., Geng, S., Zhao, H., Zhang, H., Xiong, B., Li, Z., et al. (2021). Pickering gel emulsion of lipiodol stabilized by hairy nanogels for intra-artery embolization antitumor therapy. Chem. Eng. J. *418*, 129534. https://doi.org/10.1016/j.cej.2021.129534.

39. Zhang, X.-D., Wu, D., Shen, X., Liu, P.-X., Fan, F.-Y., and Fan, S.-J. (2012). In vivo renal clearance, biodistribution, toxicity of gold nanoclusters. Biomaterials *33*, 4628–4638. https://doi.org/10.1016/j.biomaterials.2012.03.020.